01 Dec 1999

Wide-Bandwidth Multi-Resolutional Analysis of a Surface-Mounted PM Synchronous Machine

S. D. Sudhoff

Jerry L. Tichenor

James L. Drewniak
Missouri University of Science and Technology, drewniak@mst.edu

Recommended Citation

S. D. Sudhoff et al., "Wide-Bandwidth Multi-Resolutional Analysis of a Surface-Mounted PM Synchronous Machine," *IEEE Transactions on Energy Conversion*, vol. 14, no. 4, pp. 1011-1018, Institute of Electrical and Electronics Engineers (IEEE), Dec 1999.
The definitive version is available at https://doi.org/10.1109/60.815021

Wide-Bandwidth Multi-Resolutional Analysis of a Surface-Mounted PM Synchronous Machine

S.D. Sudhoff, Member, IEEE
Purdue University
West Lafayette, IN 47907-1285 USA

J.L Tichenor, J.L. Drewniak, Members, IEEE
University of Missouri - Rolla
Rolla, MO 65409-0040 USA

Abstract: Advances in power semiconductor devices have led to inverters with unprecedented voltage edge rates. This has decreased inverter switching losses and enabled the use of increasingly higher switching frequencies. However, faster edge rates and higher switching frequencies increase electromagnetic compatibility (EMC) problems, machine insulation stress, bearing currents, and other aspects of system design. Typical computer simulations used to design and evaluate proposed electric drive systems cannot be used to predict these high-frequency effects. A wide-bandwidth multi-resolutional analysis that allows designers to anticipate and quantify high-frequency effects is detailed in this paper. The approach is specifically applied to permanent magnet synchronous machine drives, and is validated experimentally.

Keywords: simulation, EMC, bearing currents, high-frequency effects, motor drives, inverters, insulation stress

I. INTRODUCTON

Power semiconductor devices are switching larger voltages and currents in increasingly shorter times. The resulting decrease in switching losses has led to smaller, less expensive inverters utilizing increasingly higher switching frequencies. New power semiconductor devices, such as MCTs and SiC based devices (due to shorter minority carrier lifetimes and higher operating voltages) promise to further increase edge rates. However, increased voltage edge rates associated with power semiconductor devices also have undesirable effects including increased common-mode currents leading to electromagnetic compatibility (EMC) problems, insulation breakdown due to inverter induced overvoltages at the machine terminals, and bearing currents in induction motor drives, to name a few [1-4].

Computer modeling of electric drives is commonly used by designers to evaluate harmonic performance, torque ripple, control algorithm functionality, etc. prior to construction. The ultimate goal of such analysis is to produce working hardware with a minimum of costly redesigns and retrofits. However, present modeling approaches are not suitable for anticipating the high-frequency effects that are responsible for many failure modes, because the models are only valid to relatively low frequencies (10's of kHz).

This paper sets forth a wide-bandwidth multi-resolutional modeling and simulation approach for a surface-mounted permanent-magnet synchronous machine (SM-PMSM). In this formulation, two modes of simulation are supported. In the standard resolution mode, the designer can utilize the standard types of time-domain simulation in order to address low-frequency (relatively speaking) issues such as current harmonics, torque ripple, and controller performance [5-6]. In the high-resolution mode, the wide-bandwidth machine model is used to predict the induced current spikes and common-mode currents associated with high voltage edge rates. The approach can be used for setting edge rates, evaluating common-mode filters, and selecting switching algorithms. The proposed method is demonstrated experimentally.

PE-153-EC-0-10-1998 A paper recommended and approved by the IEEE Electric Machinery Committee of the IEEE Power Engineering Society for publication in the IEEE Transactions on Energy Conversion. Manuscript submitted March 27, 1998; made available for printing November 10, 1998.

II. MACHINE NOMENCLATURE

Fig. 1 depicts a schematic of a surface-mounted permanent-magnet synchronous machine (SM-PMSM). The a- b- and c-phase windings are labeled a'-a, b'-b, and c'-c, respectively, and are shown as being in lumped positions although they are actually distributed around the machine in the stator slots (not shown). There are four external electrical nodes of the device. The a, b, and c nodes are the connections to the a-, b-, and c-phase windings, respectively. The other external node is the frame of the machine which is denoted f. The machine neutral is labeled n; however, this node does not have an external connection. In contrast to an induction machine, the rotor of the SM-PMSM (using ferrite or compression molded

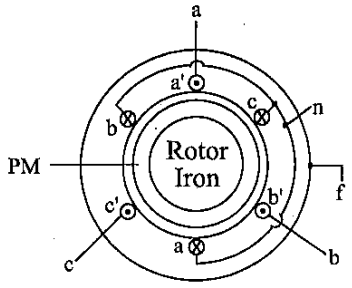

Figure 1. SM-PMSM Machine.

neodymium-iron-boron) does not have a significant effect on the high-frequency performance (though this may not be the case with samarium-cobalt or sintered neodymium-iron-boron). Consequently, the shaft is not a node in this circuit as it would be in the case of an induction machine.

In describing the operation of the machine, the voltages v_a, v_b, v_c will denote the a-, b-, and c-phase voltages applied to the machine relative to the neutral, and v_f will designate the machine's frame voltage relative to the neutral point. Currents into the a, b, c, and f nodes are labeled i_a, i_b, i_c, and i_f, respectively. The mechanical rotor position and speed are designated θ_{rm} and ω_{rm}; the electrical rotor position and speed as θ_r and ω_r, and are equal to $P/2$ times the corresponding mechanical quantities where P is the number of poles.

III. Low-Frequency Machine Model

Using Ohm's and Faraday's laws, the machine variable voltage equation is

$$\mathbf{v}_{abc} = r_s \mathbf{i}_{abc} + p\boldsymbol{\lambda}_{abc} \tag{1}$$

where p denotes differentiation with respect to time. In (1), and throughout the remainder of this work, variables of the form

$$\mathbf{f}_{a...m} = [f_a \quad \cdots \quad f_m]^T \tag{2}$$

where f may be a voltage v, current i, or flux linkage λ. The flux linkage equation for a SM-PMSM in which the relative permeability of the permanent magnet material is close to unity may be expressed

$$\boldsymbol{\lambda}_{abc} = \mathbf{L}_s i_{abc} + \boldsymbol{\lambda}_{abc,pm} \tag{3}$$

where $\mathbf{L}_s$ is a matrix with diagonal elements of the sum of the leakage inductance L_{ls} and the magnetizing inductance L_{ms} and with off diagonal elements of $-L_{ms}/2$, and where $\boldsymbol{\lambda}_{abc,pm}$ is the vector of flux linking each of three windings due to the permanent magnet. Assuming a sinusoidal back emf,

$$\boldsymbol{\lambda}_{abc,pm} = \lambda_m \left[\sin\theta_r \quad \sin\left(\theta_r - \frac{2\pi}{3}\right) \quad \sin\left(\theta_r + \frac{2\pi}{3}\right) \right]^T \tag{4}$$

In (4) λ_m is a constant determined by the strength of the permanent magnet as well as the machine and winding geometry. Using co-energy techniques, the electromagnetic torque may be expressed

$$T_e = \frac{P}{2} \frac{\partial \boldsymbol{\lambda}_{abc,pm}^T}{\partial \theta_r} \mathbf{i}_{abc}. \tag{5}$$

For the purposes of machine analysis, it is convenient to transform the machine variable based model given by (1,3,4-5) to q- and d-axis variables. The transformation between qd and abc variables is defined as

$$\mathbf{f}_{qdo} = \mathbf{K}_s \mathbf{f}_{abc} \tag{6}$$

where

$$\mathbf{K}_s = \frac{2}{3} \begin{bmatrix} \cos(\theta) & \cos(\theta - \frac{2\pi}{3}) & \cos(\theta + \frac{2\pi}{3}) \\ \sin(\theta) & \sin(\theta - \frac{2\pi}{3}) & \sin(\theta + \frac{2\pi}{3}) \\ \frac{1}{2} & \frac{1}{2} & \frac{1}{2} \end{bmatrix} \tag{7}$$

In (7), θ denotes the position of the reference frame. Selecting the rotor reference frame in which $\theta = \theta_r$, the qd and zero sequence voltage equations are

$$\mathbf{v}_{qd}^r = r_s \mathbf{i}_{qd}^r + \omega_r \begin{bmatrix} 0 & 1 \\ -1 & 0 \end{bmatrix} \boldsymbol{\lambda}_{qd}^r + p\boldsymbol{\lambda}_{qd}^r \tag{8}$$

and

$$v_0 = r_s i_0 + p\lambda_0, \tag{9}$$

respectively. The 'r' superscript in (8) denotes the rotor reference frame (the zero sequence variables do not carry a superscript since they are independent of reference frame). The corresponding qd and zero sequence flux linkage equations are

$$\boldsymbol{\lambda}_{qd}^r = (L_{ls} + \frac{3}{2} L_{ms}) \mathbf{i}_{qd}^r + \lambda_m [0 \quad 1]^T \tag{10}$$

and

$$\lambda_0 = L_{ls} i_0. \tag{11}$$

Finally, in terms of qd variables, torque may be expressed

$$T_e = \frac{3}{2} \frac{P}{2} \lambda_m i_{qs}^r. \tag{12}$$

IV. Wide-Bandwidth Machine Model

The classical model of a SM-PMSM machine with a sinuisoidal back emf was reviewed in the previous section. Although the model accurately predicts low-frequency (<20 kHz) machine behavior, it breaks down at high frequencies due to eddy currents, skin effect, and parasitic capacitances.

The proposed wide-bandwidth machine model assumes the relative permeability of the permanent magnet material is close to unity, and that the resistivity of the permanent magnet material is high. Under these assumptions there are no electrical dynamics associated with the rotor structure and so the machine's external electrical nodes are a, b, c, and f. This assumption will be shown to work well for the type of machine considered but will be removed in a future publication addressing the induction machine.

Even with the assumption that the rotor structure does not enter into the high-frequency dynamics, the development of a wide-bandwidth model is complicated by the fact that at the high end of the frequency range of interest, the machine acts as a distributed rather than lumped parameter system. One approach to incorporating this complexity into the machine model is to express the machine voltage equation as

$$\mathbf{v}_{abcf} = \mathbf{Z} \mathbf{i}_{abcf} + p\boldsymbol{\lambda}_{abcf,pm} \tag{13}$$

where the relationship between the voltages and currents is represented through the machine variable operational

impedance matrix $\mathbf{Z}$, and $\boldsymbol{\lambda}_{abcf,pm}$ is equal to $\boldsymbol{\lambda}_{abc,pm}$ augmented with a zero in the fourth element in order to maintain correct dimensionality. Due to symmetry, the machine variable operation impedance matrix has the form

$$\mathbf{Z} = \begin{bmatrix} Z_{ss} & Z_{sa} & Z_{sa} & Z_{sf} \\ Z_{sa} & Z_{ss} & Z_{sa} & Z_{sf} \\ Z_{sa} & Z_{sa} & Z_{ss} & Z_{sf} \\ Z_{sf} & Z_{sf} & Z_{sf} & Z_{ff} \end{bmatrix} \tag{14}$$

where Z_{ss} denotes the impedance between each phase and the neutral point, Z_{sa} denotes the mutual impedance between a phase and an adjacent phase, Z_{sf} denotes the mutual impedance of a phase with the frame of the machine, and Z_{ff} denotes the impedance between the frame of the machine and the neutral point. Each of these elements is of sufficient order to capture the machine dynamics over the desired frequency range.

The model may be simplified by noting that,

$$\sum_{column} \mathbf{i}_{abcf} = 0 \tag{15}$$

Incorporating (14-15) into (13) yields

$$\mathbf{v}_{abc} = Z_s \mathbf{i}_{abc} + Z_{sc} i_f [1 \quad 1 \quad 1]^T + p\boldsymbol{\lambda}_{abc,pm} \tag{16}$$

and

$$v_f = Z_f i_f \tag{17}$$

where Z_s, Z_{sc}, and Z_f are scalar operational impedance operators defined by

$$Z_s = Z_{ss} - Z_{sa} \tag{18}$$

$$Z_{sc} = Z_{sf} - Z_{sa} \tag{19}$$

$$Z_f = Z_{ff} - Z_{sf} \tag{20}$$

It was convenient to refer the low-frequency machine variable model to the rotor reference frame because it eliminated rotor position dependence from the flux linkage equations. In the case of the wide-bandwidth model, the machine variable description is transformed to the stationary reference frame. In this case, the transformation to *qd* variables explicitly extracts the zero sequence equation. The stationary reference is used instead of the rotor reference frame because the analytically awkward step of transforming a high-order operational impedance to a rotating reference frame is avoided. Transforming (16) to the stationary reference frame yields

$$\mathbf{v}^s_{qd} = Z_s \mathbf{i}^s_{qd} + {}^r\mathbf{K}^s_s \omega_r \lambda_m [1 \quad 0]^T \tag{21}$$

and

$$v_0 = Z_0 i_0 \tag{22}$$

where

$$Z_0 = Z_s - 3Z_{sc}. \tag{23}$$

In (21), ${}^r\mathbf{K}^s_s$ is the transformation from the rotor to stationary reference frame given by

$${}^r\mathbf{K}^s_s = \begin{bmatrix} \cos\theta_r & \sin\theta_r \\ -\sin\theta_r & \cos\theta_r \end{bmatrix}. \tag{24}$$

It is necessary to consider the machine connections to the inverter to proceed further; these are depicted in Fig. 2. Therein, all lead impedance is lumped into the machine model (though this is not necessary in general) and Z_{fg} represents the machine frame-to-ground (node g) impedance. The voltage source v_{r-g} represents the voltage from the lower rail (node r) to the ground bus (a '-x' in a subscript denotes that this voltage is relative to the node 'x' instead of the machine neutral). If the lower rail is the ground bus, then v_{r-g} is zero; or if the ground bus splits the source voltage v_{r-g} is $-v_{dc}/2$. From Kirchoff's voltage law

$$-\mathbf{v}_{abc-r} + \mathbf{v}_{abc} + (v_{f-g} - v_f - v_{r-g})[1 \quad 1 \quad 1]^T = 0 \tag{25}$$

Multiplying (25) by $\mathbf{K}_s$ it can be shown that

$$\mathbf{v}_{qd} = \begin{bmatrix} 1 & 0 & 0 \\ 0 & 1 & 0 \end{bmatrix} \mathbf{K}_s \mathbf{v}_{abc-r} \tag{26}$$

Summing the elements of the vector valued (25),

$$-\sum_{column} \mathbf{v}_{abc-r} + 3v_0 - 3v_f + 3v_{f-g} - 3v_{r-g} = 0. \tag{27}$$

From Fig. 2,

$$v_{f-g} = -Z_{fg} i_f. \tag{28}$$

Incorporating (17),(22), and (28) into (27),

$$v_{cm} = Z_{cm}\, i_{cm}, \tag{29}$$

where the common mode voltage is defined as

$$v_{cm} = \frac{1}{3} \sum_{column} \mathbf{v}_{abc-r} + v_{r-g}, \tag{30}$$

the common-mode current as

$$i_{cm} = -i_f = 3i_0, \tag{31}$$

and the common-mode operational impedance as

$$Z_{cm} = \frac{1}{3} Z_0 + Z_f + Z_{fg}. \tag{32}$$

Together, (21), (26), (29) and (30) form a wide-bandwidth

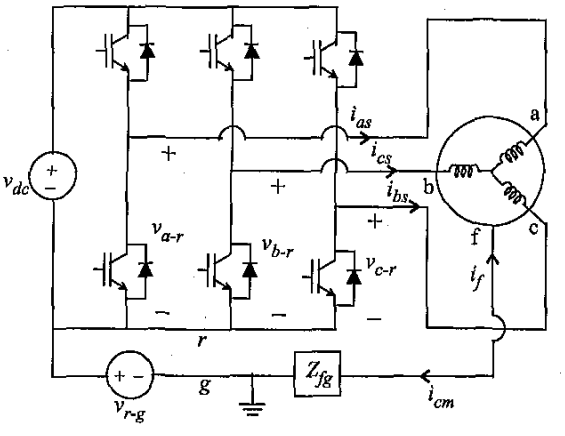

Figure 2. Inverter connections.

model of the PMSM. The inputs to this model are the line-to-rail voltages v_{abc-r} and the rail-to-ground voltage v_{r-g}. The outputs are the q- and d-axis currents i^s_{qd} and the common mode current i_{cm}.

V. Implementation

Although the machine model of the previous section is sufficient to capture the machine behavior, it is computationally cumbersome because of numerical stiffness. Integration algorithms for stiff systems (such as Gear's) are not as effective in solving power electronics based systems as in other applications because the power-electronic switching periodically excites high-frequency dynamics. As a result, the computation time to reach steady-state operating conditions is undesirably long.

The difficulties associated with model stiffness may be eliminated by using a multi-resolution approach in which the simulation has two modes: a low-resolution mode (LRM) in which a standard low-frequency model is used, and a high-resolution mode (HRM) in which all the dynamics are represented. The transition between the two modes can be made nearly seamless.

The first step in developing such an approach is to reconsider the low-frequency model. In particular, substituting (10) into (8) and then transforming from the rotor reference frame to the stationary reference frame yields

$$\mathbf{v}^s_{qd} = \hat{Z}_s \hat{\mathbf{i}}^s_{qd} + {}^r\mathbf{K}^s_s \omega_r \lambda_m [1 \quad 0]^T . \tag{33}$$

In (33), $\hat{\mathbf{i}}^s_{qd}$ is an estimate for the q- and d-axis currents using the low-frequency model, and $\hat{Z}_s$ is the low-frequency approximation to Z_s given by

$$\hat{Z}_s = r_s + (L_{ls} + \tfrac{3}{2} L_{ms}) p . \tag{34}$$

Subtracting (33) from (21) yields

$$\Delta \mathbf{i}^s_{qd} = G_{HF} \hat{\mathbf{i}}^s_{qd} \tag{35}$$

where $\Delta \mathbf{i}^s_{qd}$ is the error in the low-frequency model and

$$G_{HF} = Z_s^{-1} \hat{Z}_s - 1 . \tag{36}$$

This suggests the simulation strategy depicted in Fig. 3. Therein, the electrical inputs to the machine simulation are the phase-to-lower rail voltages $\mathbf{v}_{abc-r}$ and the lower rail-to-ground voltage v_{r-g}. Using (26) with $\theta = \theta_r$ yields the qd voltage vector $\mathbf{v}^r_{qd}$, which is an input to the standard low–frequency model described by (8-11). The low-frequency model is used to calculate $\hat{\mathbf{i}}^r_{qd}$ (the current that would flow if the low-frequency model were valid over the entire frequency range) which is then used to calculate torque (12), which can in turn be used to calculate the mechanical dynamics.

The currents calculated from the low-frequency model are also used to determine the error in the currents due to neglecting the high-frequency dynamics. If the simulation is in high resolution mode (HRM), then the signal path of Switch 1 is in the HRM position, whereupon $\hat{\mathbf{i}}^s_{qd}$ is calculated from $\hat{\mathbf{i}}^r_{qd}$ using the frame-to-frame transformation (24), and is used as an input to the high-frequency correction dynamics G_{HF}, which yields the current error $\Delta \mathbf{i}^s_{qd}$. This error term is transformed to the rotor reference frame and added to $\hat{\mathbf{i}}^r_{qd}$ to give the corrected qd current vector $\mathbf{i}^r_{qd}$.

To implement the model, G_{HF} must be converted to state-space form; controller canonical form is convenient for this purpose. An important aspect of this is that when the simulation is in the low-resolution mode (LRM) all derivatives associated with the implementation of G_{HF} are set to zero, thereby eliminating all fast dynamics.

The common-mode dynamics are only included when the simulation is in the high-resolution mode. In this case, the common-mode voltage is calculated based on the phase-to-ground voltages $\mathbf{v}_{abc-r}$ and line-to-ground voltage v_{r-g}. The common-mode dynamics captured in Z_{cm} are used to calculate the common-mode current i_{cm}, from which the zero-sequence current i_o is also readily obtained. As in the case of the qd-axis dynamics, when converting the model to a time-domain representation, the inverse operational impedance Z_{cm} is converted to controller canonical state-

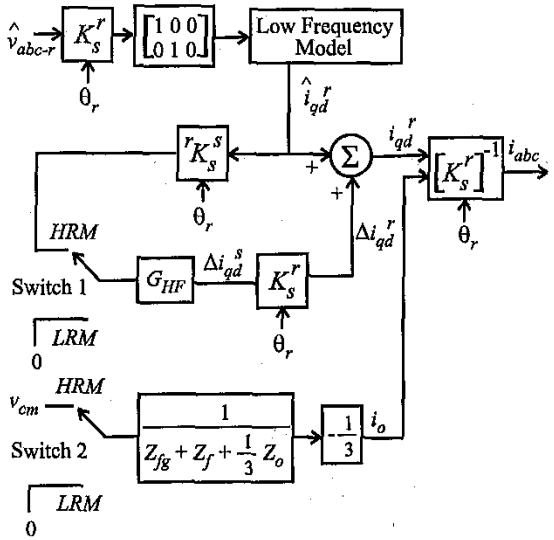

Figure 3. Wide-bandwidth multi-resolutional simulation structure.

space form, and when the simulation is in the low-resolution mode all derivatives associated with the common-mode current dynamics are set to zero.

A feature of interest in Fig. 3 is the computation of the electromagnetic torque T_e. In the proposed simulation structure, torque is always calculated using the low-frequency current estimate. Although it would be tempting to replace $\hat{i}_q^r$ by i_q^r in (12) for calculating torque, the distribution of the current at high-frequencies is different than assumed in the derivation of (12). Furthermore, zero-sequence current could interact with the 3rd harmonic of the back-emf waveforms (which can be neglected in the low-frequency model due to the wye-connection), leading to another source of error. Thus, the benefit of replacing $\hat{i}_q^r$ by i_q^r in (12) is unclear.

VI. Machine Characterization

The first step in determining the machine parameters necessary to use the proposed modeling approach is to determine the parameters of the low-frequency model. These may be obtained using a variety of well-known methods. For the studies presented herein the test machine is a commercial unit with a rated speed of 3000 rpm and a rated torque of 1.81 Nm. The measured low-frequency machine parameters are $P=4$, $r_s=2.99\ \Omega$, $L_{ss}=11.35$ mH ($L_{ls}+3L_{ms}/2$), and $\lambda_m=0.156$ Vs.

The next step is to determine G_{HF}. First the impedance Z_s, which is equal to either the q-axis or d-axis operational impedance of the machine, is measured using established techniques [7]. Theoretically, in SM-PMSMs the q- and d-axis impedances should be identical; they are very close in the test machine. The magnitude of the measured operational impedance $Z_d = Z_s$ is shown in Fig. 4. For low frequencies (< 10 kHz) this impedance looks like a simple RL circuit. However, at 30 kHz there is a parallel resonance after which the machine looks capacitive. As frequency is further increased, the machine eventually looks inductive again after a series resonance at 7 MHz.

Once Z_s is measured, G_{HF} is established using (36). The magnitude of G_{HF} is depicted in Fig. 5 for the test machine, along with the fitted transfer function used to represent this data. When fitting a polynomial transfer function to this characteristic, it is important that the form of the polynomial be such that

$$G_{HF}(0) = 0, \tag{37}$$

which can be insured by requiring G_{HF} be of the form

$$G_{HF} = \frac{a_1 s + a_2 s^2 + \cdots + a_m s^m}{1 + b_1 s + b_2 s^2 + \cdots + b_n s^n} \tag{38}$$

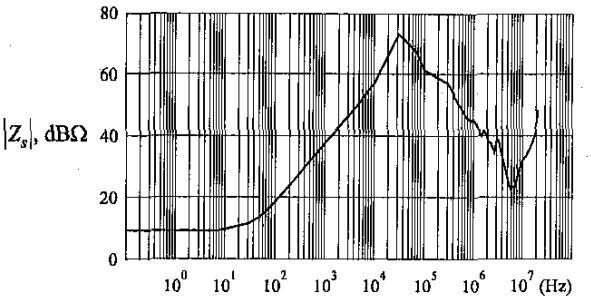

Figure 4. Machine stator impedance.

where $m \le n$. The fit can be accomplished in a number of ways; herein, the curve is fitted using quadratic optimization. An important choice in fitting G_{HF} is the frequency range of the data points used in determining the parameters. As shown in Fig. 5, for frequencies below 10 kHz, G_{HF} is very small, and so accuracy is not critical below this frequency. The high frequency bound is determined by balancing bandwidth and a suitable polynomial fit of reasonable order. For the test machine, the upper bound was 10 MHz. The fitted G_{HF} for the test machine is given by

$$G_{HF} = \frac{1.741246 \cdot 10^{-8} s + 1.108269 \cdot 10^{-16} s^2}{1 + 3.255244 \cdot 10^{-8} s + 5.550438 \cdot 10^{-16} s^2}. \tag{39}$$

The common mode impedance was also measured and curve fitted. This impedance was measured by disconnecting the a-, b-, and c- phase lead connections from the inverter, connecting them together, and measuring the impedance between this common node and the ground node. The common mode impedance for the test machine, along with the fitted characteristic, is shown in Fig. 6. For the purpose of an operational impedance representation of the measured data, it is convenient to express the common mode impedance as

$$Z_{cm} = \frac{c_0 + c_1 s + \cdots + c_o s^o}{s + d_2 s^2 + \cdots + d_p s^p} \tag{40}$$

where $o \ge p$ so that the inverse is proper. This form insures that at low frequencies the common mode impedance tends towards infinity as the frequency goes to zero in accordance

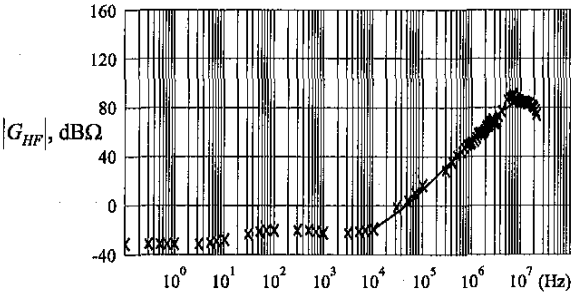

Figure 5. High-frequency correction transfer function.

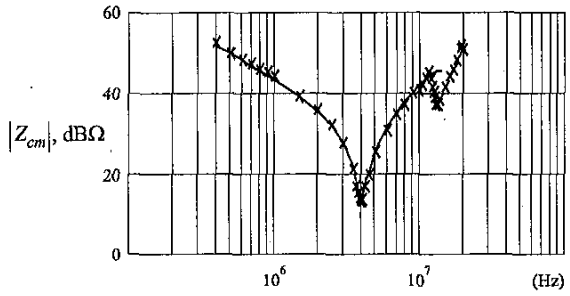

Figure 6. Common mode impedance and fitted representation.

with the series capacitive coupling which exists in the common-mode circuit.

$$Z_{cm}(s) = \frac{9.90041\cdot 10^{8} + 1.22928\cdot 10^{1} s + 1.58860\cdot 10^{-6} s^{2} + 1.261455\cdot 10^{-14} s^{3}}{s + 8.92613\cdot 10^{-10} s^{2} + 1.422388\cdot 10^{-16} s^{3}} \quad (41)$$

VII. Inverter Model

In order to capture high-frequency effects of a motor drive, it is necessary to utilize a high-frequency model of the inverter as well. Ideally, such a model would include either detailed physics-based or behavioral models of the inverter semiconductors [8], any EMI filtering, as well as the parasitics associated with the inverter layout. Because the focus of this paper is the analysis of the machine, a simpler approach of ramping the line-to-rail voltage of each leg between initial and final values was used herein. For this purpose, let t_{sw} denote the time at which the supervisory controls command a change in switch status. The line-to-ground voltage is then ramped from its initial value (either 0 or v_{dc}) to its final value (either v_{dc} or 0) starting at time t_1 and ending at time t_2, where t_1 and t_2 are a function of the type of transition (high-to-low or low-to-high) and the polarity of the phase current at the instant the change in state of the switch command occurs. These times are tabulated in Table 1. Therein, $1\rightarrow 0$ and $0\rightarrow 1$ denote transitions from the upper semiconductor on to the lower one on and vice-versa, respectively, and i denotes the current out of a given phase leg (i_{as}, i_{bs}, or i_{cs}).

In Table 1, t_{don} represents a delay from the instant a change in switching command is issued until a change in leg voltage occurs for the case in which the leg current will be transferred from a flyback diode to an active switch. It includes logic propagation delay, dead-time circuit delay, and delay associated with the semiconductors themselves. The time t_{on} represents the approximate time it takes for the current to transfer from the diode to an active switch after the change in voltage begins. The times t_{doff} and t_{off} are similarly defined, except they apply to the case in which current is transferred from a controllable semiconductor to a diode.

Table 1. Inverter Leg Representation

	$1\rightarrow 0, i>0$	$1\rightarrow 0, i<0$	$0\rightarrow 1, i>0$	$0\rightarrow 1, i>0$
t_1	$t_{sw}+t_{doff}$	$t_{sw}+t_{don}$	$t_{sw}+t_{don}$	$t_{sw}+t_{doff}$
t_2	t_1+t_{off}	t_1+t_{on}	t_1+t_{on}	t_1+t_{off}

The experimental test system used for model validation was based on a FUJI 6MBI30L-060 three-phase bridge inverter driven using FUJI EXB-840 base drive circuits. The measured values of t_{don}, t_{on}, t_{doff}, and t_{off} were 2.95 μs, 60.4 ns, 2.15 μs, and 0.17 μs, respectively. These times represent averages over many transitions.

VIII. Experimental Validation

Figs. 7-11 illustrate measured and simulated current waveforms for the SM-PMSM test motor. In this study, a q-axis supervisory control [5] with delta-modulated switching control [6] was used, with the exception that the delta-modulator was designed such that the three-phase legs switch in sequence separated by 1/3 of the switching period. The machine was operating at 3000 rpm with a 1.72 Nm torque command. The inverter was operating at a dc link voltage of 300 V and 30.3 kHz switching frequency.

Fig. 7 depicts the a-phase current as measured and as predicted using the multi-resolutional simulation in low-resolution mode. The measured and experimental results compare well; however, the high-frequency machine behavior is not represented (nor could even be seen on this time scale). This mode of simulation is useful for establishing an operating point.

A transition can be made to the high-resolution mode at any point in the simulation to examine the high-frequency system behavior. Fig. 8 depicts a small segment of the approximately sinusoidal current in the region of the positive zero crossing. The segment is so short that the low-frequency

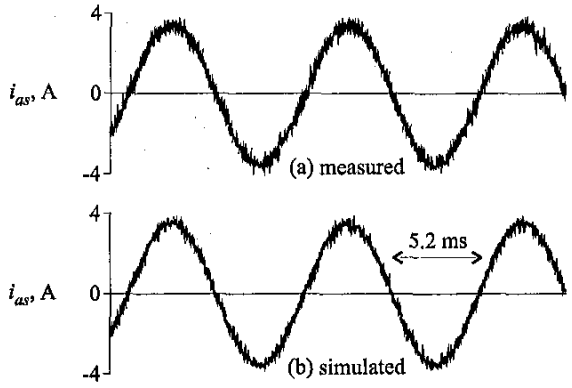

Figure 7. Low-resolution mode a-phase current.

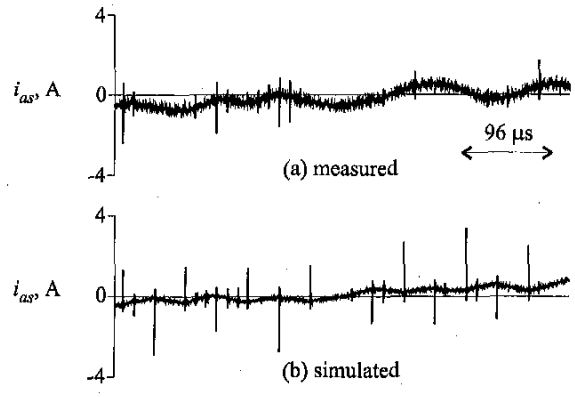

Figure 8. A-phase current near positive zero crossing.

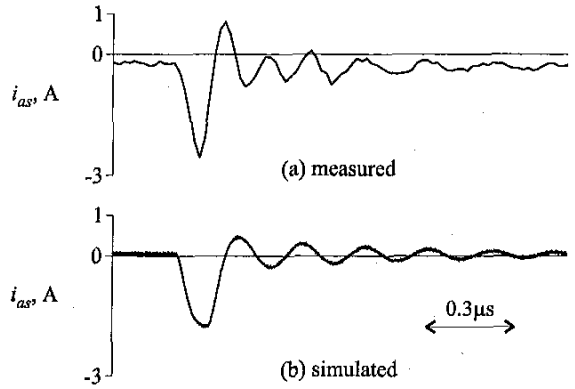

Figure 9. A-phase current (expanded time scale).

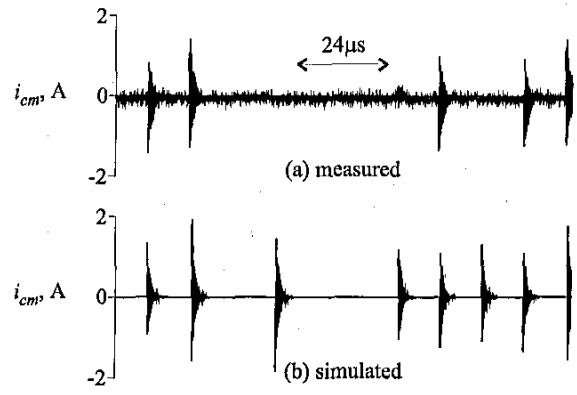

Figure 10. Common mode current.

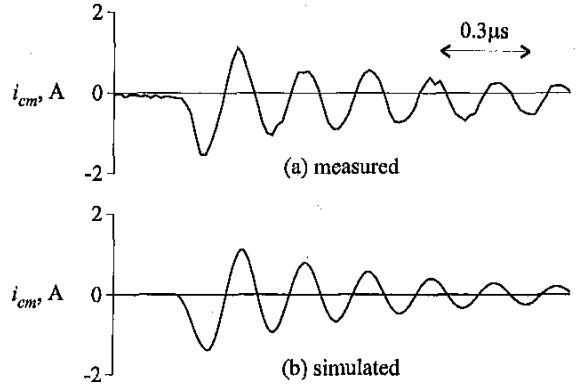

Figure 11. Common mode current (expanded time scale).

component of the current looks essentially linear over the interval considered. The switching sequence is asynchronous, so the exact sequence of switching never repeats – either in the simulation or in the actual system. For this reason, in some sense the comparison is qualitative. However, the simulation predicts the same variety of high frequency current spikes that are observed in the actual system. Fig. 9 illustrates typical measured and simulated a-phase current waveforms on a more expanded time scale. Although not an exact match, (which is not be expected since the initial conditions are not exactly the same and the inverter representation is highly simplified) the correspondence between the simulation results and the measurements is good.

One difference which can be observed between the measured and simulated waveforms is the level of very high frequency 'fuzz' in the measured and experimental results. This difference has no physical significance. In the case of the experimental results, this is measurement noise (notice that on the expanded time scale it disappears). In the case of the simulated results, the noise is numerical and has to do with Gears algorithm trying to maximize the time step. The amount of numerical noise is a function of the bounds placed on the time step as well as the order and relative speed of the dynamics being simulated.

Figs. 10 and 11 depict the measured and simulated common-mode current on a reduced and expanded time scale. Again, the switching sequence in the simulation in not identical to the experimental test system; however, it is clear that simulation closely emulates the measured behavior. Notice that in this case no numerical noise is present in the simulated waveforms.

The simulation speed in low-resolution mode is 7.6 times slower than real time on a Sun Ultra 2 CPU using the 4th order Runga-Kutta integration algorithm (re-initialized on every switching event) with a 0.1 ms time step. In the high-resolution mode, the simulation is 85,000 times slower than real time on the same CPU using Gear's algorithm with a 10^{-9} s to 10^{-20} s variable time step. Although slow, this is not prohibitive since the amount of time simulated in high-resolution mode is short. This is possible because low-resolution mode is used to find the desired operating point. For example, generating Fig. 8 (including establishing the initial operating point) only required 51 s of CPU time. This is an advantage of the multi-resolutional approach.

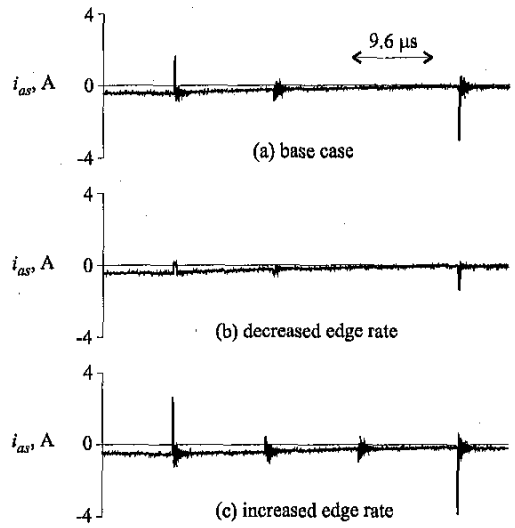

Figure 12. A-phase current for different edge rates.

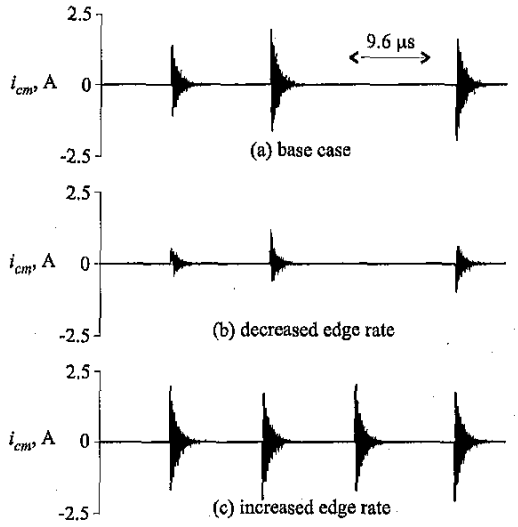

Figure 13. Common mode current for different edge rates.

IX. Design Tradeoff Example

The machine model presented herein can be used in component and system design to explore system behavior as various parameters are varied. As an example, the effect of changing the inverter edge rate is depicted in Figs. 12-13. Therein, the phase and common-mode current waveforms that result from the base case (same as Figs. 8-11) from decreasing the edge by a factor of three, and by increasing them by a factor of three are shown. Decreasing the edge rate decreases the severity of both the phase and common mode current spikes, as expected. However, increasing the edge rate only significantly increases the amplitude of the phase current spike, not the common-mode current spike. This is a result of the fact that for the test drive base case, the inverter slew rates were already so fast that the voltage waveforms could nearly be considered a step. The observation that the phase current underwent a relatively larger increase than the common-mode current is explained by considering that while the common-mode impedance has a resonant minimum at 4 MHz the phase impedance has a resonant minimum at 6 MHz and is therefore more sensitive to increasing the edge rate.

X. Conclusion

Numerous problems have been related to high-frequency effects such as common-mode currents, overvoltages at the machine terminals, and bearing currents (particularly in induction machines). A wide-bandwidth analysis of SM-PMSM drive has been set forth in order to provide design guidance with respect to high-frequency effects in this type of drive. The use of a multi-resolutional formulation of the method provides a computationally efficient analysis of these systems by only incorporating the high-frequency dynamics when required. The analysis has been experimentally verified and shown to be accurate. Future publications will show the extension of the method necessary to predict transmission line effects and the associated overvoltages at the machine terminals, the application of the method to the induction motor and the prediction of bearing currents, as well as a method to estimate the high-frequency machine parameters from geometrical design data.

XI. References

[1] S. Chen, T.A. Lipo, D. Fitzgerald, "Source of induction motor bearing currents caused by PWM inverters," *IEEE Trans. on EC*, Vol. 11, March 1996.

[2] P. Langhorst and C. Hancock, "The simple truth about motor-drive compatibility," Magnetek application notes.

[3] A. von Jouanne, P.Enjeti, W.Gray, "The Effect of Long Motor Leads on PWM Inverter Fed AC Motor Drive Systems", IEEE Applied Power Electronics Conference 1995, pp. 592-597.

[4] R.J. Kerkman, "Twenty Years of PWM AC Drives: When Secondary Issues Become Primary Concerns", Proceedings of the 1996 IEEE IECON. 22nd International Conference on Industrial Electronics, Control, and Instrumentation, Vol. 1, pp. LVII-LXII.

[5] S.D. Sudhoff, K.A. Corzine, and H.J. Hegner, "A Flux-Weakening Strategy for Current-Regulated Surface-Mounted Permanent Magnet Machine Drives," *IEEE Trans. on EC*, Vol. 10, No. 3, Sept. 1995, pp. 431-437.

[6] K.A. Corzine, S.D. Sudhoff, "A Hybrid Observer for High Performance Brushless DC Drives," *IEEE Trans. on EC*, Vol. 11, No. 2, June 1996, pp. 318-323.

[7] IEEE Std. 115A-1987.

[8] J.T. Tichenor,S.D. Sudhoff, J.L. Drewniak, "Behavioral IGBT Modeling for Prediction of High Frequency Effects in Motor Drives," 1997 Naval Symposium on Electric Machines Proceedings, July 28-31, 1997, Newport RI, pp. 69-75.

XII. Acknowledgements

This work was supported by the University of South Carolina grant no. N00014-96-1-0926 with ONR.

Scott D. Sudhoff is an Associate Professor of Electrical and Computer Engineering at Purdue University. Jerry L. Tichenor is a Research Engineer at the University of Missouri –Rolla James L. Drewniak is an Associate Professor of Electrical Engineering at the University of Missouri – Rolla.